Author/s:
Harrison, KD;Sales, E;Hiebert, BD;Panahifar, A;Zhu, N;Arnason, T;Swekla, KJ;Pivonka, P;Chapman, LD;Cooper, DML

Title:
Direct Assessment of Rabbit Cortical Bone Basic Multicellular Unit Longitudinal Erosion Rate: A 4D Synchrotron-Based Approach

Date:
2022-11-01

Citation:
Harrison, K. D., Sales, E., Hiebert, B. D., Panahifar, A., Zhu, N., Arnason, T., Swekla, K. J., Pivonka, P., Chapman, L. D. & Cooper, D. M. L. (2022). Direct Assessment of Rabbit Cortical Bone Basic Multicellular Unit Longitudinal Erosion Rate: A 4D Synchrotron-Based Approach. Journal of Bone and Mineral Research, 37 (11), pp.2244-2258. https://doi.org/10.1002/jbmr.4700.

Persistent Link:
https://hdl.handle.net/11343/335944

RESEARCH ARTICLE

JBMR®

Direct Assessment of Rabbit Cortical Bone Basic Multicellular Unit Longitudinal Erosion Rate: A 4D Synchrotron-Based Approach

Kim D Harrison,[1] Erika Sales,[1] Beverly D Hiebert,[1] Arash Panahifar,[2,3] Ning Zhu,[2] Terra Arnason,[4] Kurtis J Swekla,[5] Peter Pivonka,[6] L Dean Chapman,[1] and David ML Cooper[1]

[1]Department of Anatomy, Physiology and Pharmacology, College of Medicine, University of Saskatchewan, Saskatoon, Canada
[2]BioMedical Imaging and Therapy Beamline, Canadian Light Source, Saskatoon, Canada
[3]Department of Medical Imaging, College of Medicine, University of Saskatchewan, Saskatoon, Canada
[4]Department of Medicine, College of Medicine, University of Saskatchewan, Saskatoon, Canada
[5]Animal Care and Research Support Office, Office of the Vice President of Research, University of Saskatchewan, Saskatoon, Canada
[6]School of Mechanical, Medical, and Process Engineering, Queensland University of Technology, Brisbane, Australia

ABSTRACT

Cortical bone remodeling is carried out by basic multicellular units (BMUs), which couple resorption to formation. Although fluorochrome labeling has facilitated study of BMU formative parameters since the 1960s, some resorptive parameters, including the longitudinal erosion rate (LER), have remained beyond reach of direct measurement. Indeed, our only insights into this spatiotemporal parameter of BMU behavior come from classical studies that indirectly inferred LER. Here, we demonstrate a 4D in vivo method to directly measure LER through in-line phase contrast synchrotron imaging. The tibias of rabbits ($n = 15$) dosed daily with parathyroid hormone were first imaged in vivo (synchrotron micro-CT; day 15) and then ex vivo 14 days later (conventional micro-CT; day 29). Mean LER assessed by landmarking the co-registered scans was 23.69 ± 1.73 μm/d. This novel approach holds great promise for the direct study of the spatiotemporal coordination of bone remodeling, its role in diseases such as osteoporosis, as well as related treatments. © 2022 The Authors. *Journal of Bone and Mineral Research* published by Wiley Periodicals LLC on behalf of American Society for Bone and Mineral Research (ASBMR).

KEY WORDS: BONE MICRO-CT; SYNCHROTRON RADIATION; CORTICAL POROSITY; BASIC MULTICELLULAR UNIT; LONGITUDINAL EROSION RATE

Introduction

Bone is a highly dynamic tissue, continuously altering its microarchitectural properties in response to environmental and mechanical stressors.[1] Through the process of remodeling, tissue turnover is carried out by specialized cellular groupings first described as basic metabolizing units[2-4] and later, more commonly referred to as basic multicellular units (BMUs) [5] (Fig. 1). In cortical bone, localized resorption by the BMU's osteoclastic cutting cone creates a cylindrical tunnel or remodeling space. In classical descriptions, this is followed by a quiescent reversal zone where resorption has ceased but formation has yet to start.[6] Recent studies have revealed this region actually reflects a mixed reversal-resorption phase where osteoprogenitor expansion and osteoclastic radial resorption of the BMU co-occur until, it is postulated, a cellular density threshold of osteoprogenitor cells is reached and formation is initiated by osteoblasts.[7] This final, formative phase of the BMU takes the form of a closing cone, filling the remodeling space with mineralizing osteoid around a contracting central vascular canal. The structural products of remodeling in cortical bone, Haversian systems (synonymous with secondary osteons), permeate and vascularize the mineralized matrix; thus, BMUs are essential for the lifelong maintenance and optimization of bone material

Received in original form September 28, 2021; revised form August 16, 2022; accepted September 3, 2022.
Address correspondence to: David ML Cooper, PhD, Department of Anatomy, Physiology and Pharmacology, College of Medicine, University of Saskatchewan, 107 Wiggins Rd, Saskatoon, SK, S7N 5E5, Canada.
E-mail: dml.cooper@usask.ca
Additional Supporting Information may be found in the online version of this article.
DMLC is supported by the Canada Research Chairs program, Canadian Institutes of Health Research, Natural Engineering and Research Council of Canada, and Social Sciences and Humanities Research Council of Canada.

Journal of Bone and Mineral Research, Vol. 37, No. 11, November 2022, pp 2244–2258.
DOI: 10.1002/jbmr.4700

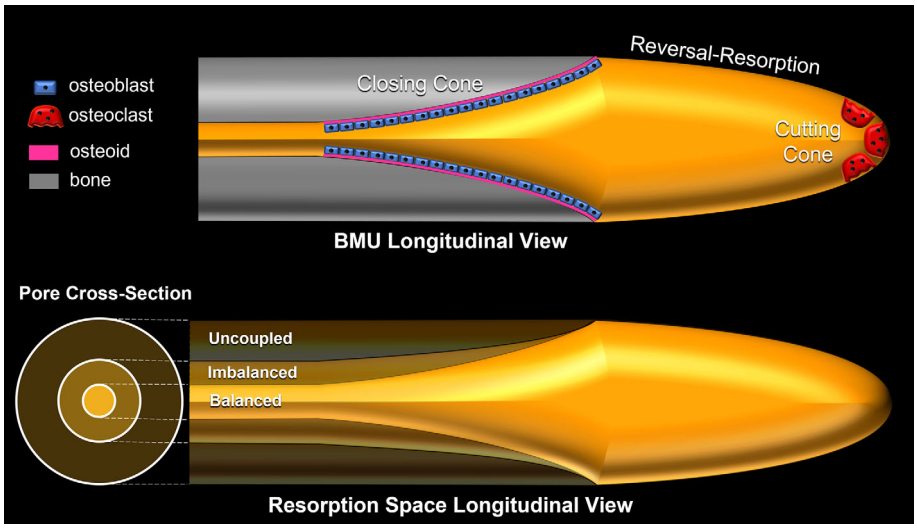

Fig. 1. Basic multicellular unit (BMU) morphology and remodeling states. Schematic view of the BMU in cortical bone (top) and its relation to porous structures (remodeling space and persisting vascular canal = orange) in the balanced, imbalanced, and uncoupled states (bottom).

properties and microarchitecture. Under normal conditions, the resorptive activities of the BMU are spatially and temporally "coupled" to its formative activities, and the extent of each is balanced (Fig. 1). Bone loss, such as that observed in osteoporosis (OP), occurs when remodeling becomes imbalanced (ie, resorption outweighing formation)[8,9] or uncoupled (ie, arrest within the reversal zone with no subsequent bone formation).[7,10,11] In the cortex, net bone loss, summed across a multitude of individual BMUs, is manifested as increased cortical porosity and trabecularized or thinned cortices,[12,13] leading to fragile, brittle bones, which are much more susceptible to fracture.[14,15] Of particular concern is that increased porosity inherently creates a larger intracortical surface for further remodeling to occur upon.[16] Worldwide, hundreds of millions are afflicted with OP, and the costs reach into the billions[17]; however, despite the daunting scale of these human and economic impacts, we know relatively little about the spatiotemporal (3D over time, or 4D) regulation of BMU activity and this deficit is particularly acute for cortical bone. Although OP research has traditionally focused on trabecular bone loss (mass and density), the cortex is increasingly understood to be a site of significant bone loss and fracture.[18]

The 4D behavior of BMUs has not been replicated in vitro and has never been directly observed in vivo. Consequently, what we currently know about coordination of cortical remodeling is derived from relatively few 3D serial/sequential sectioning studies of both trabecular and cortical bone,[10,11,19-25] which generate data that are inherently static in nature. Dynamic insight into BMU activity via fluorochrome (eg, tetracycline) labeling of bone formation was pioneered more than 50 years ago by Frost, one of the most influential researchers to shape the field of skeletal biology.[26] Over his illustrious career, Frost's contributions were unequivocal, and perhaps his most influential work was defining the BMU as a unified, regulatory intermediary unit (between the level of cell and tissue) that dictates the coupling of bone resorption with formation. Although the formative activities of the BMU could be tracked over time using Frost's innovative approach—including in 3D when combined with serial sectioning[27]—a similar assessment of the resorptive phase could not. A key example, and focus of the current study, is the longitudinal erosion rate (LER)—the rate of advance of the BMU cutting cone over time. To date, LER has only ever been *inferred* in a few species (Fig. 2), yielding measurements ranging from 20 to 44 μm/d (Fig. 2; Table 1).

Jaworski and Lok,[28] for example, relied upon the assumption of a constant distance from the tip of the cutting cone back to a fluorochrome label (mineralizing osteoid) or, similarly, the cutting cone matching the advance of the osteoid seam beyond a label for their LER measures, whereas Takahashi and Norimatsu[30] inferred LER from the advance of the closing cone (bone formed between two labels), assuming it was synchronized with the cutting cone advance. After decades, these pioneering studies remain our only assessments of LER, with the value of ~40 μm/d all but treated as a constant across skeletal elements, species, and disease states (Table 1). Indeed, many in silico studies use this value for analyzing different aspects of BMU behavior. For example, Buenzli and colleagues[31] used LER of 40 μm/d to investigate the spatiotemporal distribution of osteoclastic and osteoblastic cell populations in the BMU at different maturation stages. They found that the precursor cells in the reversal zone play a crucial role in separating the cutting cone and closing cone. Furthermore, their model predicted that perturbing the biochemical environment in the BMU may lead to imbalanced remodeling, which has been subsequently confirmed experimentally. A follow-up cortical bone study by Buenzli and colleagues[32] looked at in silico modeling of individual osteoclastic resorption events that are responsible for the shape of the BMU cutting cone. For that study, the rate of blood vessel growth in the BMU, which produces osteoclastic precursor cells, was assumed to be 40 μm/d, which led to a LER of similar magnitude. A study by Ryser and colleagues[33] looked at removal of microcracks by BMUs and the potential of a single BMU to change its path in order to target microcracks/bone matrix damage. The latter work utilized a LER of 40 μm/d.

Treating LER as a constant is highly problematic as: (i) the original data from canines showed a great deal of variation,

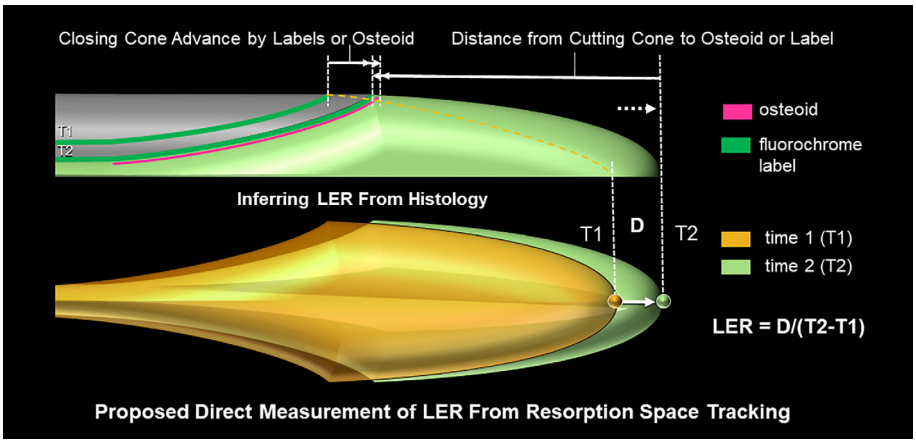

Fig. 2. Assessment of basic multicellular unit (BMU) longitudinal erosion rate (LER) in cortical bone. Classical indirect method for inferring BMU LER from fluorochrome labeling of the closing cone (top) and the novel proposed direct method of measuring advancement of the cutting cone using in vivo imaging and image registration (bottom).

undermining the very assumptions the measurements were based upon[28,30]; (ii) synchronicity of the phases of the BMU cannot be taken as a given—particularly in light of recent concepts focused on the role of uncoupling in bone loss; and (iii) even the classical studies provide evidence that LER could vary in disease states such as uremia, where it was depressed in afflicted versus normal dogs.[29] Moreover, the extremely limited data available for humans appears to suggest lower LER values relative to other species (extrapolated by Parfitt[6] from published and unpublished data). Given all the problematic assumptions in these classical studies and the enduring gaps in our knowledge, the larger significance of LER in BMU remodeling and diseases such as OP remains unclear. It is an open question whether LER could play a role in BMU coupling. For example, is uncoupling associated with the faster advance of the closing cone, resulting in a larger reversal-resorption zone and decreased time for the critical threshold of osteoprogenitors to be reached[7,25]? Might the converse be true with a lower LER improving coupling and overall balance of BMU activity? Could modulation of LER present a new avenue for interventions aimed at preventing or reversing bone loss? These questions have remained unanswered as we lack a direct means to assess LER in vivo.

Around the turn of the millennium, X-ray micro-computed tomography (micro-CT) underwent rapid development, seeing use first ex vivo and soon after in vivo for trabecular bone imaging and structural analysis. The latter has included longitudinally tracking changes at the level of individual trabeculae over time.[34,35] Although the translation of this technology to cortical bone porosity occurred relatively early,[36] the translation to in vivo cortical porosity imaging in preclinical models has been relatively rare,[37,38] being impeded by the need for higher resolution and, concomitantly, higher radiation dose. Indeed, repetitive in vivo trabecular bone protocols with typical image resolutions of 9 to 18 μm[39-41] and radiation doses in the range of 0.5 to 1 Gy are known to cause adverse effects, such as reduced bone volume fraction in the tibiae of mice.[39,41-43] In vivo synchrotron radiation (SR) scans of 13-week-old mice's knees at a dose of 5 Gy have also reported adverse effects on trabecular bone 10 days post scan.[44] In X-ray tomography, resolution is inversely proportional to radiation dose, and the

Table 1. Summary of Classical Studies of Longitudinal Erosion Rate (LER)

Publication	Species	Element	LER (μm/d)	Age	Sex
Jaworski and Lok[28]	Dog	Rib	39.2 ± 14	1 year	Male
Jaworski et al.[29]	Dog (uremic)	Rib	27.97 ± 0.8	1 year	Male
Jaworski et al.[29]	Dog	Rib	43.61 ± 0.66	1 year	Male
Takahashi et al.[30]	Dog	Rib	40.8 ± 15.0	Adult	Male
Takahashi et al.[30]	Dog	Humerus	34.9 ± 13.3	Adult	Male
Takahashi et al.[30]	Dog	Radius	34.7 ± 13.5	Adult	Male
Takahashi et al.[30]	Dog	Ulna	32.9 ± 11.7	Adult	Male
Takahashi et al.[30]	Dog	Femur	39.2 ± 13.5	Adult	Male
Takahashi et al.[30]	Dog	Tibia	37.0 ± 13.2	Adult	Male
Takahashi et al.[30]	Dog	Fibula	42.6 ± 26.0	Adult	Male
Parfitt[a(6)]	Monkey	Rib	36.7	N/A	N/A
Parfitt[b(6)]	Human	Rib	27.0	N/A	N/A

[a]Unpublished data from Oliver and Crouch.

[b]Human LER calculated based on the assumption that cortical remodeling between humans and monkeys is similar and thus, measures such as radial erosion rate are interchangeable between species.[6]

relationship is not linear—doubling resolution involves 16 times the dose if image quality is to be maintained,[45] and multiple scans further exacerbate this over time.[46] Thus, although micro-CT is certainly capable of resolving cortical bone porosity in preclinical animal models, including BMU-related remodeling spaces, in vivo tracking of these spaces has not been attempted. A potential solution to circumvent the punishing relationship between resolution and dose is through X-ray phase contrast SR micro-CT.[47] In conventional X-ray imaging, the contrast mechanism is absorption of X-rays by tissue, which equates directly to dose. Exploiting the phase contrast created by the refraction and/or scattering of X-rays rather than absorption within a sample creates the opportunity for improved contrast at equivalent or even potentially lower doses. This principle works particularly well for imaging cortical bone porosity with SR micro-CT, where there is a significant difference in the refractive indices between bone and the soft tissue within its pores.[48,49]

Beyond radiation dose limitations associated with imaging, an additional challenge is the need for an animal model that exhibits cortical remodeling similar to that observed in humans. Notably, small rodents such as the mouse and rat have very small vascular canals within their cortices that are not only challenging to image in vivo but, most critically, these species exhibit little or no cortical remodeling.[50,51] The rabbit is the smallest laboratory animal with cortical bone remodeling similar to humans,[49,52-54] and we previously reported several interventions capable of elevating cortical remodeling in the rabbit, including parathyroid hormone (PTH) dosing, ovariohysterectomy (OVH), glucocorticoid (GC) dosing, and combined GC + OVH.[49] Of note, while this study reported ovariectomy (OVX) was performed, it has since been confirmed surgery was actually ovariohysterectomy (OVH). PTH exhibited the most dramatic increase in remodeling rate, and this protocol was selected for the current study. Here our primary objective was to deploy SR micro-CT to directly track the LER of cortical BMUs in vivo for the first time. To achieve this, we developed a novel approach at the BioMedical Imaging and Therapy (BMIT) facility of the Canadian Light Source (CLS) synchrotron focused on the PTH-dosed rabbit model. Secondarily, we explored the potential impact of varied radiation dose (1, 2.5, and 5 Gy) on LER and other outcomes, basing this range upon values reported in the literature.

Materials and Methods

Animals

Fifteen skeletally mature, 6-month-old (3.7 to 3.9 kg) female New Zealand White rabbits were acquired from Charles River Laboratories (Quebec, Canada). Animals were housed individually in stainless-steel rabbit racks in the University of Saskatchewan's Health Sciences Laboratory Animal Services Unit, a Canadian Council on Animal Care (CCAC)-accredited facility. A computerized system controlled room temperature and humidity, and the light cycle was maintained at 12:12 (12 hours dark and 12 hours of light). Standard rabbit chow, alfalfa cubes, and reverse osmosis water via an automated watering system were provided *ad libitum*. Animals were acclimatized for a minimum of 7 days before any experimental procedures commenced. All animal work was carried out under animal use protocol (AUP 20170068), which was approved by the University of Saskatchewan's Animal Care Committee and adhered to the CCAC guidelines for humane animal use.

PTH rabbit model of elevated remodeling

While rabbits do exhibit spontaneous cortical bone remodeling, the rate of remodeling or activation frequency (Ac.f—birth rate of new BMUs [#/mm^2/year]) is low; thus, we sought to increase the number of BMUs available for LER analysis through daily dosing with human PTH 1 - 34 (Alfa Aesar, Ward Hill, MA, USA), a known elevator of cortical remodeling/porosity within rabbits.[49,55-58] The intermittent PTH rabbit model used in this study, as previously described by our group, results in a dramatic increase in remodeling rate (14.2-fold increase in activation frequency over sham controls).[49] Briefly, each rabbit received a daily dose (via subcutaneous injection) of human PTH$^{(1\text{-}34)}$ at a concentration of 30 µg/kg/d for 28 days. Animals were monitored daily at the time of injection, as well as weekly to assess weight. Weights were measured once before dosing commenced (day 0) and once weekly thereafter until the last week (day 25). The fluorochrome calcein (Sigma Aldrich, St. Louis, MO, USA) was administered by subcutaneous injection at a dose of 10 mg/kg on days 15 and 16 (label 1) and then on days 27 and 28 (label 2) of the treatment period to facilitate dynamic histomorphometry. Imaging (see below) was performed in vivo on day 15. After the dosing period was complete (day 28), animals were euthanized on day 29 by intravenous injection of pentobarbital sodium (Euthanyl; Bimeda-MTC, Animal Health Inc, Cambridge, Canada) at a dose of 0.4 mL/kg. Post-euthanasia, the right and left tibias were removed, dissected of soft tissue, and fixed in 10% formalin ahead of ex vivo laboratory micro-CT imaging.

In vivo SR micro-CT imaging protocol

All in vivo scans were acquired on the BMIT 05ID-2 beamline at the CLS synchrotron (Saskatoon, Canada). Rabbits were anesthetized before imaging according to an established protocol using a transnasal delivery of a sedative and anesthetic cocktail (dexmedetomidine [0.1 mg/kg], midazolam [2.0 mg/kg], and torbugesic [0.4 mg/kg]) and supported during imaging via inhaled isoflurane gas.[59] During scanning, the rabbits were restrained in a custom holder adapted from a design by Voor and colleagues.[60] An indirect X-ray detector system composed of a C11440-22CU Orca Flash 4.0 camera paired with an AA60 beam monitor (Hamamatsu Photonics, Hamamatsu, Japan) and LuAG:Ce 200-µm-thick scintillator was used to achieve an effective pixel size of 13.05 µm at the sample location. Source-to-sample distance was 58 m and sample-to-detector distance was 60 cm, the latter distance being chosen to impart in-line phase contrast to the projection images and subsequently reconstructed tomograms. The monochromatic X-ray beam was produced by a superconducting wiggler operated at 2.5T, passed through a 3.3-mm Al filter, and selected at 37.5 keV energy by the double bent Laue monochromator (Si 1,1,1). Potential radiation dose effects were assessed by dividing animals into 3 groups of 5, each imaged at approximately 1 (low), 2.5 (medium), and 5 (high) Gy. These doses were chosen based upon preliminary experiments with rats where we employed 2.5 Gy[48] dose with no apparent short-term (eg, 2 weeks) radiation-induced side effects and the dose of 5 Gy, a level where in vivo synchrotron imaging has been previously reported to induce negative effects on trabecular morphology over a time frame (10 days).[44] The scans were acquired as the animals underwent continuous rotation through 180 degrees and no shuttering was employed. The dose rate

was determined by the storage ring current (peak of 250 mA after electron injection with subsequent decay) and Lucite (poly(methyl methacrylate) [PMMA]) filters (80 to 120 mm). The dose rate was measured in air at the beam entrance into the experimental hutch in real time using a PinPoint ion chamber (model 31014, PTW, Freiburg, Germany). The surface dose at the sample position is based on the Inverse Square Law and was calculated using the formula: $I_1/I_2 = D^2_2/D^2_1$, where D_1 is the distance from the source to the beam entrance into the hutch and D_2 is the source to sample distance. I_1 and I_2 are the beam intensity (dose) at D_1 and D_2, respectively. In addition, to solve for I_2, the surface dose at the target, attenuation through air and the animal holder (made of PMMA) needs to be considered using the formula $I_2 = I_1 e^{[(\mu_{air} \cdot X_{air}) + (\mu_{PMMA} \cdot X_{PMMA})]}$. Mass attenuation coefficients (μ/ρ) at 37.5 keV were taken from NIST (https://physics.nist.gov/) and were used to derive linear attenuation coefficients (μ). For air, the distance between ion chamber and animal (X_{air}) was 648 cm, density (ρ_{air}) is considered 0.001293 g/cm^3, and linear attenuation coefficient (μ_{air}) is 0.000324141 cm^{-1}. For PMMA, thickness (X_{PMMA}) was 0.3 cm, density (ρ_{PMMA}) is 1.18 g/cm^3, and $\mu_{(PMMA)}$ is 0.2904 cm^{-1}. The calculated dose rate was experimentally confirmed by placing the ion chamber at the animal location. Environmental conditions (ie, temperature, humidity, and air pressure) were corrected for final reporting of the dose. The dose rate at the animal location at 37.5 keV is approximately 42% smaller than the dose rate at the hutch entrance, when considering the distance through air, thickness of PMMA, and inverse square of the distance. The rotation speed required to achieve the desired incident surface dose was calculated factoring in the dose rate (Gy/s) at animal location. Scan times varied from 40 to 60 seconds with rotational speeds thus varying between 3 and 4.5 degrees/second. The higher doses of 2.5 and 5 Gy enabled the collection of 1500 projections as opposed to 1000 for the 1 Gy group. The estimated imaging doses were confirmed experimentally through thermoluminescent dosimeter (TLD) chips (Mirion Technologies, Concord, Canada). Each TLD chip was placed at the mid-field of view (FOV) corresponding to the location of the in vivo scans. Fifteen chips (five/dose group) were imaged, in vivo, with the full in vivo protocol (including the initial vertical scout scan, described below) and revealed an average radiation dose of 0.9, 2.4, and 5.4 Gy for the low, medium, and high groups, respectively. Based upon additional TLD measures in a subsequent study with matching conditions for the medium radiation dose, scattered dose to the body of the rabbits (including the non-imaged limb) was measured to be 0.30 mGy from which linear scaling can estimate values of 0.12 and 0.60 mGy for the low and high radiation doses, respectively.

The FOV was approximately 1 cm high and 2.6 cm wide, which readily encompassed the width of the distal tibia. A vertical scout scan (~8 cm) of the right tibial diaphysis was taken before the rotational scan to locate the anatomical landmark, the plafond, from which the stage would be raised 2 cm to demark the start position of the in vivo scan. Vertical scout scans ensured consistent identification of the FOV of cortical bone within individual rabbits for subsequent ex vivo scans but also among all the rabbits. Post imaging, the rabbits were injected intramuscularly with the anesthetic reversal drugs atipamezole (1 mg/kg) and flumazenil (0.02 mg/kg) and monitored in a warmed recovery cage until fully recovered. For the 2 weeks post in vivo imaging (days 15 to 28), rabbits were monitored daily for indications of radiation impacts through visual inspection of both the imaging site (ie, skin burns, hair loss) and overall health (ie, loss of appetite, behavioral changes, grooming changes, defecation quality, and consistency).

Ex vivo micro-CT imaging protocol

Post euthanasia (day 29), both the previously in vivo (day 15) imaged right and contralateral control left tibias from each rabbit were removed and dissected of soft tissue. To help facilitate scan co-registration, the FOV of the right tibia scanned in vivo was identified on the same bone, ex vivo, with a single (2 cm) and double (3 cm) cut mark proximal to the plafond to denote the bottom and top of the FOV, respectively. Ex vivo scans were collected with a SkyScan 1172 desktop micro-CT scanner (Bruker, Kontich, Belgium). The FOV between the cut marks was imaged at 74 kVp and 133 μA with an exposure time of 460 ms, 0.2° rotation step through 180 degrees, 4-frame averaging, Al 0.5 mm filter, and voxel size of 4.93 μm.

Data reconstruction

The projectional data (both in vivo SR micro-CT and ex vivo micro-CT) were reconstructed using the NRecon software package (Bruker) using conventional filtered back-projection. For the SR micro-CT data, phase retrieval was not employed and thus the resulting images were, similar to the micro-CT data, dominated by absorption contrast and with similar imaging energies (monochromatic X-rays of 37.5 keV for SR micro-CT and energy spectrum peak of 34 keV and estimated mean energy of 40.9 keV for micro-CT) with the addition of edge enhancement yielding improved detection of the porosity.[48] Both sets of data were generated as 8-bit bitmaps with their histograms matched to facilitate standardized segmentation by a global threshold consistent with that of our previous study,[49] which was calibrated by a phantom to 1.13 g/cm^3 hydroxyapatite. This is a slightly different approach from the previous analysis of these data and an exploration of the impact on the outcomes (which proved marginal) is presented in Supplemental Fig. S1. After reconstruction, the ex vivo data were binned by 3D averaging (2×2) to 9.86 μm using the software package Tconvert (Bruker) to reduce the size of the data set and thereby facilitate scan co-registration.

Scan co-registration and LER measurement

Scan co-registration and BMU LER measurement were performed using AMIRA (version 2020.2; https://www.thermofisher.com/amira-avizo). A schematic of the approach is provided in Supplemental Fig. S2. The in vivo SR micro-CT and ex vivo micro-CT scans of the right tibia for each rabbit were rendered in 3D (Fig. 3, left), and the BMU-related remodeling spaces and vascular canals were segmented using the standard global threshold (Fig. 3, center). After segmentation, the 3D volume render of the in vivo SR micro-CT scan was manually aligned (translated and rotated) within the single- and double-cut marks of the 3D volume rendering of the ex vivo micro-CT scan and then automatically co-registered by AMIRA's Affine Registration Module using rigid translation and rotation combined with isotropic scaling. Registration was performed on the raw grayscale data sets and convergence was based upon the correlation metric of this AMIRA module. The segmented porosity was then visually inspected to verify the fit of the co-registration between the two data sets. Vascular canals that had not changed between scans

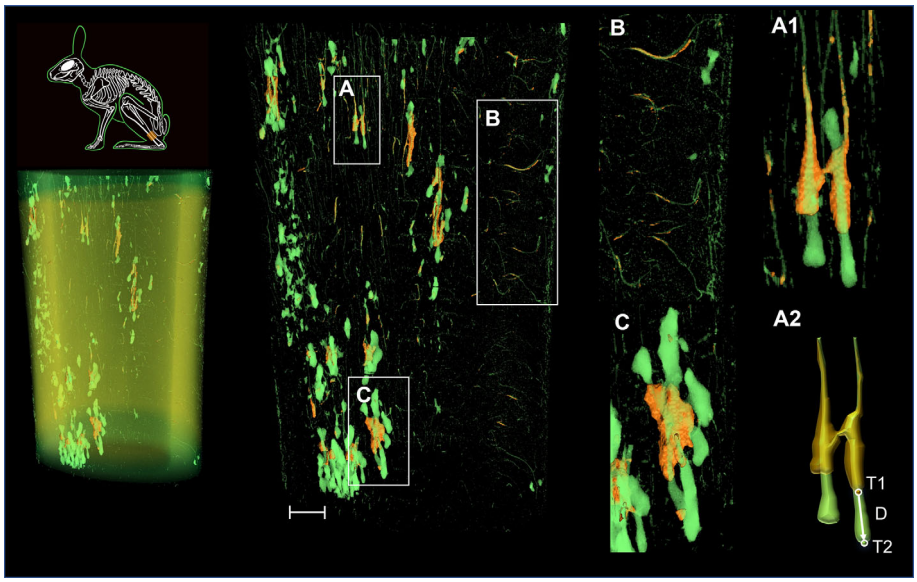

Fig. 3. Longitudinal erosion rate (LER) assessment based on synchrotron radiation (SR) micro-CT and micro-CT co-registered scans. (Top left) Rabbit skeletal schematic displaying region of the distal tibia scanned (transparent, orange square). (Bottom left) The in vivo SR micro-CT scan (translucent orange render) at time 1 (T1, day 15) is co-registered within the ex vivo micro-CT scan (translucent, green render) from time 2 (T2, day 29). (Center) Cortical porosity rendered alone revealing (*A*) classically shaped basic multicellular unit (BMU)-related resorption spaces, (*B*) unchanged vascular canals, and (*C*) complex irregular BMU-related resorption spaces. (Right) Zoomed-in views (*A1*, *B*, *C*) from central panel and (*A2*) a schematic depiction of the direct method of LER assessment where LER = D/T2-T1, where D denotes the distance between the tips of the cutting cones (in μm) and T2-T1 denotes the time difference between the two scans (ie, 14 days). Scale bar = 1 mm.

served as natural biological fiducial markers. If the match was poor, careful manual positioning was performed followed by a repeat of the automatic registration. Surface renders of the cutting cones of an individual BMU were then manually landmarked (Fig. 3, right; A2), yielding 3D coordinates: X1, Y1, Z1 (tip of the cutting cone in vivo) and X2, Y2, Z2 (tip of the cutting cone ex vivo). LER (μm/day) was calculated as D/T2-T1, where $D = \sqrt{(X2-X1)^2+(Y2-Y1)^2+(Z2-Z1)^2}$ and denotes the distance between the tips of the cutting cones (in μm) and T2–T1 denotes the time difference between the two scans (ie, 14 days) (Fig. 3, right; A2). For 3 of the 15 scan sets, regions of extensive PTH-induced clustered porosity caused co-registration failure (Fig. 4E). For the 12 successfully registered data sets, reproducibility of the registration was explored by repeating the registrations three times each and calculating precision as the root-mean-square average of the standard deviation of the transform parameters.[61]

Cortical porosity and geometry measurement

Assessment of potential in vivo radiation-related impacts on cortical bone remodeling was performed on the corresponding 1 cm longitudinal FOV region of the distal diaphysis in the imaging software package CTAnalyser (CTAn; version 1.16.4.1; Bruker). The FOV was binarized using the standard global threshold to measure cortical porosity (Ct.Po, %), mean canal diameter (Ca.Dm, μm; a measure analogous to trabecular thickness[36]), and cortical thickness (Ct.Th, μm) in 3D. In correspondence with the previous study by our group,[49] a single, midpoint slice of the 1 cm region of bone was selected to analyze total area (T.Ar, mm^2), cortical area (Ct.Ar, mm^2), and marrow area (Ma.Ar, mm^2) in 2D. This same process was also carried out on the left tibia of each rabbit.

Dynamic histomorphometry

Histological assessment of cortical remodeling parameters was conducted as described in our previous study.[49] Briefly, confocal microscopy (Leica Microsystems, Wetzlar, Germany) was used to image undecalcified cross sections (cut by diamond wafer saw and polished to 150 μm) extracted from the proximal end of the imaged FOV. Bright-field and fluorescence images were analyzed using ImageJ (https://imagej.nih.gov/ij/). Single-labeled osteons (sL.On), double-labeled osteons (dL.On), and resorption cavities (Rs.N) were manually counted and normalized to Ct.Ar (sL.On/Ct.Ar, dL.On/Ct.Ar, and Rs.N/Ct.Ar, mm^{-2}). The ratio of labeled osteons to resorption cavities ([sL.On + dL.On]/Rs.N) was also calculated from these data. Activation frequency (Ac.f) was calculated as Ac.f = ([sL.On+dL.On]/Ct.Ar)/σf (#/mm^2/yr), where σf, the osteon formation time, was calculated as W.Th/On.MAR. Osteon wall thickness (W.Th) was measured as the distance between the osteon canal and cement line in 20 randomly selected osteons from each section. Osteonal mineral apposition rate (On.MAR, μm/d) was calculated as the inter-label distance of up to 20 randomly selected dL.On, divided by the labeling period (12 days). One animal in each dose group had no detectable double-labeled osteons and thus On.MAR and Ac.f could not be calculated for them. Finally, active remodeling centers

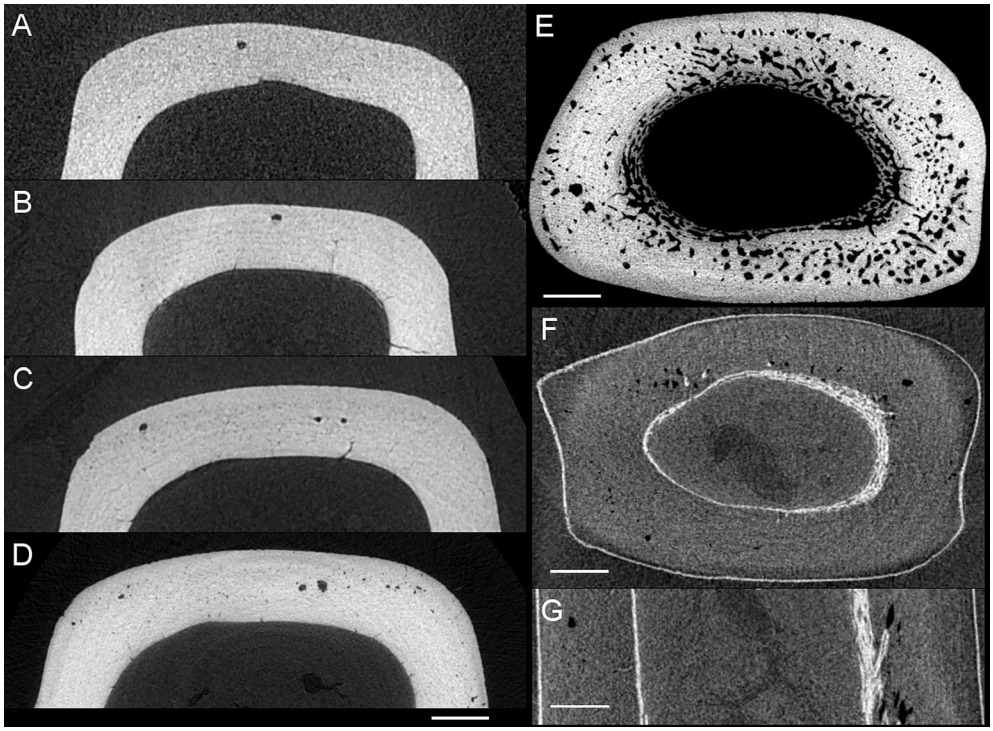

Fig. 4. Representative 2D images depicting tibias from different animals scanned in vivo (day 15) at low (1 Gy, *A*), medium (2.5 Gy, *B*), and high (5 Gy, *C*) radiation dose. A roughly matching (eg, raw image before any registration) ex vivo image of the same animal depicted in (*C*) is provided in (*D*). Large basic multicellular unit (BMU)-related resorption spaces are evident in all four images. (*E*) A representative image from one of the animals that could not be successfully registered because of the extensive intracortical remodeling as well as endosteal bone formation. Subtractive images for another specimen calculated after registration are presented in (*F*) and (*G*), representing cross-sectional and longitudinal sections, respectively. Bone formation and resorption between the two scans are represented as bright and dark shades, respectively. Structures in common appear in shades of gray because of slight variations in gray intensity between the scans. Endosteal bone formation is evident in both views and an advancing BMU with new resorption at the cutting cone and trailing bone formation of the closing cone is present in (*G*).

(a.Rm.Cr, mm^{-2}) was calculated as (sL.On + dL.On + Rs.N)/Ct.Ar.

Statistical analysis

Statistical analyses were performed with SPSS version 27.0 (IBM, Armonk, New York). All measures were tested for normality by Shapiro–Wilk tests. One-way ANOVA ($\alpha = 0.05$) was used to assess LER, which had normally distributed outcomes. Comparisons of the imaging and histomorphometric outcomes categorized by scan type (right in vivo SR micro-CT versus right ex vivo micro-CT and right ex vivo micro-CT versus contralateral left ex vivo micro-CT) were carried out through repeated measures ANOVA ($\alpha = 0.05$) if normally distributed. In no cases were the main effect (eg, scan or side) as well as the interaction with radiation dose group significant and thus post hoc tests were not pursued. For parameters where at least one dose group was non-normal, the nonparametric Wilcoxon signed-rank test ($\alpha = 0.05$) was employed to make pairwise comparisons. Pooled weights at day 0 and day 25 were normally distributed and compared with a paired *t* test ($\alpha = 0.05$); however, comparison of weights among the three dose groups over the PTH dosing period (4 weeks) was not normally distributed and thus these pairwise comparisons were assessed with the nonparametric Friedman test ($\alpha = 0.05$).

Results

Scans co-registration and LER assessment

Active cortical remodeling was readily apparent in the image data sets as increased intracortical porosity and, in particular, large BMU-related remodeling spaces (Figs. 3 and 4; Supplemental Fig. S4). The varying quality of the different in vivo (day 15) scan radiation doses was visually apparent (see Supplemental Fig. S4 for quantitative assessment of image quality), with the low-dose group appearing the most noisy and progressive improvement as dose increased (Fig. 4*A–C*; Supplemental Fig. S5). The appearance of the ex vivo data was superior in terms of resolution (eg, detection of small pores). Co-registration of the data sets in general revealed excellent matches between the scans (Figs. 3 and 4; Supplemental Fig. S3; Supplemental Table S1), with close agreement between unchanged vascular canals and the paths of BMUs being trackable in many cases. Subtraction of the two registered data sets (Fig. 4*F*, *G*) provided additional confirmation of the precision of the co-registration with structures in common represented as gray, new resorption after the in vivo (day 15) scan represented as black, and new bone formation, both intra-cortically through remodeling and at the surfaces through modeling, represented as white. The patterns of bone formation observed in the subtraction images

Table 2. Direct Calculation of Basic Multicellular Units (BMU) Longitudinal Erosion Rate (LER) for Varied Radiation Dose (1, 2.5 and 5 Gy)

		Pooled	Low dose (1 Gy)	Medium dose (2.5 Gy)	High dose (5 Gy)
Parameter	ANOVA *p*	Mean ± SD	Mean ± SD	Mean ± SD	Mean ± SD
LER (μm/d)	730	23.69 ± 1.73	24.20 ± 1.65	23.15 ± 2.05	23.75 ± 1.83

Assessment of BMU LER across dose groups (low dose, medium dose, and high dose) and pooled for all 12 rabbits. LER is reported as mean ± standard deviation. One-way ANOVA was employed to compare the dose groups ($\alpha = 0.05$).

matched well with the fluorescence calcein-labeled confocal (histological) images (Supplemental Fig. S4). The overall extent and nature of remodeling varied from classically shaped BMUs to extensive complex and irregular patterns, which precluded co-registration in 3 cases (one animal from each dose group; Fig. 4*E* is from one of the excluded animals). LER was assessed for 186 BMUs from the 12 successfully co-registered data sets (4/group, ~12.4 BMUs/rabbit), and results are summarized in Table 2 and Fig. 5. There were no differences in LER between any of the dose groups, and thus pooled LER was calculated to be 23.69 ± 1.73 μm/d.

Right tibias: in vivo (day 15) versus ex vivo (day 29) scans

Comparisons between the in vivo (day 15) and ex vivo (day 29) scans of the right tibias reflected changes within the animals over time, as well as potential differences due to varied scan parameters (SR micro-CT versus micro-CT). Measurements of cortical porosity and geometry are summarized in Table 3 and Fig. 6. Overall, variation between animals was considerable, as reflected by the numerous outliers in the box plots (Fig. 6). The only consistently significant difference observed across all dose groups was a decline in Ma.Ar at day 29, associated with increased C.Th in the low-dose ($p = 0.043$) and high-dose ($p = 0.043$) groups. Ct.Po was increased at day 29 for the medium-dose ($p = 0.043$) and high-dose groups ($p = 0.043$) and the latter also had elevated Ca.Dm ($p = 0.043$). The distribution of Ca.Dm values by % of pore volume averaged within scans and limbs is included in Fig. 7. The bimodal distributions revealed a large percentage of the pore volume was composed of smaller and fragmented canals with many at the detection limits of the resolution (particularly for the in vivo scans) and, conversely, a peak in canal diameters around 80 to 120 μm created by the BMU-related remodeling spaces.

Right versus left tibias: ex vivo (day 29) scans

Comparisons between the ex vivo (day 29) scans reflected potential differences between the limbs of the same animals due to the in vivo radiation dose previously imparted to the right tibia 2 weeks prior before the left contralateral limb. Measurements of the 3D and 2D parameters are summarized in Table 4 and Fig. 6. Again, a great deal of variation was observed, with many outliers apparent in the box plots (Fig. 6) and few, if any, clear patterns emerged. The only difference observed was lower Ca.Dm ($p = 0.043$) in the in vivo scanned right tibias of the high-dose group. The distributions of Ca.Dm for the right and left ex vivo scans were more similar to each other than to the in vivo scans, reflecting the matched time point and scan parameters.

Dynamic histomorphometry

Analysis of the calcein-labeled ground sections, presented in Table 5 and Fig. 7, compared the right previously in vivo imaged tibias versus the contralateral left to assess potential impacts of the radiation dose. The right tibias had lower rates of remodeling as reflected by reduced Ac.f ($p = 0.004$), a.Rm.Cr/Ct.Ar ($p = 0.006$), and dL.On/Ct.Ar ($p = 0.001$); however, this outcome must be considered cautiously as all these measures are related to double-labeled osteons (dL.On), which indicates there were already differences between the sides at the time of the in vivo imaging as label 1 was introduced the same day (day 15). Notably, other parameters related to bone formation, On.MAR ($p = 0.727$), and resorption, Rs.N/Ct.Ar ($p = 0.171$), did not differ between sides.

Animal weight

A two-tailed, paired *t* test analysis of day 0 and day 25 revealed weight loss overall ($p = 0.019$), although a nonparametric

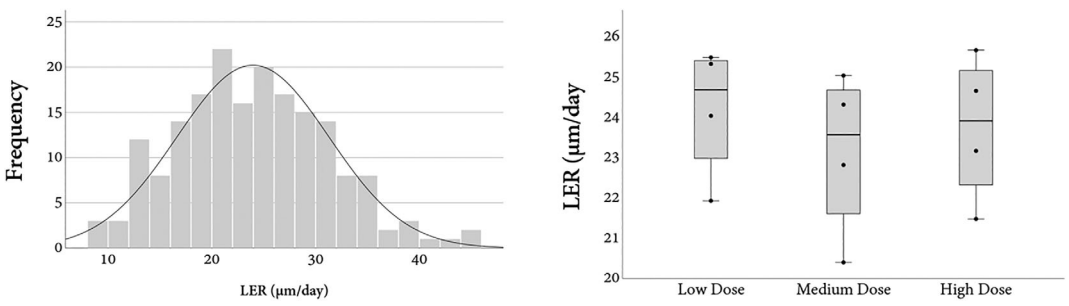

Fig. 5. Direct assessment of basic multicellular unit (BMU) longitudinal erosion rate (LER) across dose groups. Individual LER measurements pooled across animals and groups ($n = 186$) were normally distributed (left) and mean LER data by group (right) are presented by box plots with the mean values from individual rabbits plotted as solid circles ($n = 4$ rabbits/group). One-way ANOVA revealed no differences between radiation dose groups ($\alpha = 0.05$).

Table 3. Right Tibia Micro-CT Data: Comparison of In Vivo Versus Ex Vivo Scans

			Right in vivo versus right ex vivo									
			Low dose (1 Gy)				Medium dose (2.5 Gy)			High dose (5 Gy)		
			Mean ± SD (median)				Mean ± SD (median)			Mean ± SD (median)		
Parameter	ANOVA *p* side (right in vivo versus right ex vivo)	ANOVA *p* interaction (side × dose)	Wilcoxon-signed rank *p*	R. in vivo	R. ex vivo	Wilcoxon-signed rank *p*	R. in vivo	R. ex vivo	Wilcoxon-signed rank *p*	R. in vivo	R. ex vivo
Ct.Po (%)	—	—	0.080	1.06 ± 0.31 (1.09)	2.93 ± 1.48 (2.68)	0.043*	1.99 ± 1.28 (1.73)	6.94 ± 5.67 (3.85)	0.043*	1.78 ± 2.10 (1.16)	3.29 ± 1.97 (3.09)
Ca.Dm (μm)	—	—	0.500	62.36 ± 16.27 (63.17)	70.65 ± 12.15 (73.52)	0.500	78.82 ± 7.22 (78.69)	72.94 ± 25.62 (57.23)	0.043*	90.08 ± 8.70 (90.49)	72.49 ± 8.78 (68.21)
Ct.Th (μm)	—	—	0.043*	1296.33 ± 127.89 (1228.56)	1389.13 ± 149.67 (1316.81)	0.138	1346.66 ± 83.96 (1357.98)	1426.34 ± 161.32 (1412.85)	0.043*	1343.67 ± 138.76 (1286.81)	1449.65 ± 164.37 (1387.88)
Tt.Ar (mm^2)	0.101	—	—	31.16 ± 1.49	31.07 ± 1.40	—	33.16 ± 4.12	33.00 ± 4.56	—	34.60 ± 4.28	34.51 ± 4.57
Ct.Ar (mm^2)	<0.001*	—	—	20.30 ± 1.54	21.09 ± 1.34	—	21.66 ± 1.80	23.56 ± 2.63	—	22.54 ± 3.40	23.58 ± 4.00
Ma.Ar (mm^2)	—	—	0.043*	10.86 ± 1.84 (10.39)	9.98 ± 1.76 (9.76)	0.043*	11.50 ± 2.93 (10.66)	9.44 ± 2.48 (8.44)	0.043*	12.06 ± 1.73 (11.93)	10.93 ± 1.62 (10.42)

Bone parameters compared between the in vivo SR micro-CT (day 15) and ex vivo micro-CT (day 29) scan data for the (right) tibiae by dose group (n = 5). Values are reported as mean ± standard deviation. Median values are also reported for those parameters where at least one dose group was not normally distributed. For normal data, repeated measures ANOVA was employed to compare the right in vivo vs. right ex vivo tibiae results across the radiation dose groups. For non-normal data, Wilcoxon signed-rank tests were employed to compare the right in vivo vs. right ex vivo tibiae results categorized by radiation dose group. Significance (*) level was $\alpha = 0.05$ for all tests. 3D measures are Ct.Po = Cortical Porosity; Ca.Dm = Canal Diameter; and Ct.Th = Cortical Thickness; 2D measures are Tt.Ar = Total Area; Ct.Ar = Cortical Area; and Ma.Ar = Marrow Area

Friedman test observed no difference in weight among the three dose groups ($p = 0.270$) at day 25.

Discussion

Our primary goal was to establish a novel method to directly measure BMU LER in 4D within the cortical bone of rabbits using phase contrast SR micro-CT. The successful 4D co-registration of the in vivo SR micro-CT and ex vivo micro-CT scans revealed BMUs advanced an average of 23.69 μm/d or 332 μm over the 14 days between the two scans. We found considerable variance in LER across the individual BMUs (depicted in Fig. 5), and the underlying cause of this variation is unclear. An important caveat is that our approach almost certainly captured BMUs at different points in their life cycles with some just beginning to advance, some operating in a stable fashion, and some coming to an end. Indeed, examination of the registered data sets revealed new BMUs arising between scans and some resolving. As discussed, comparative data are limited and consist of inferred values (Table 1), with previously reported mean LER of ~40 μm/d coming from two studies that histologically assessed 52[28] and 58[30] BMU closing cones from three and five assumingly healthy, adult male dogs, respectively. Less cited are the results of 36.7 μm/d in monkeys[6] and 27.0 μm/d in humans (extrapolated from published and unpublished data[6]). Albeit speculative, our smaller mean LER could be due to differences between species, the type of bone analyzed, age differences,[28] or within-species microarchitectural cortical bone variation. Nevertheless, the proposed method here is the first approach for standardized tracking of BMUs in 4D in the same animals.

We also cannot rule out the potential impacts of supraphysiological PTH dosing in our rabbit model. Across the dose groups, mean Ct.Po from the right and left micro-CT scans ranged from 2.93% to 6.94%, which aligns with recent reports of varied Ct.Po among PTH-treated rabbits.[49,55,58] Visually, micro-CT cross sections revealed minor to moderate endosteal bone formation throughout the majority of the three dose groups (Fig. 4E–G; Supplemental Fig. S3), with a few instances of extensive endosteal formation observed within rabbits from both the high ($n = 1$) and medium ($n = 2$) radiation dose groups. This likely explained the higher, albeit nonsignificant ($p = 0.212$), Ct.Po values (6.93%, right and 6.94%, left) observed within the medium-dose group in comparison to those of the low-dose (2.93%, right and 3.04%, left) and high-dose (3.29%, right and 4.30%, left) groups. In rabbits, treatment with intermittent PTH has been associated with increased endosteal bone formation[49,55-57,62] that appears to mimic the anabolic bone effects observed in human skeletons when PTH is administered therapeutically. When observed, endosteal bone formation was present in both the in vivo imaged right and contralateral left control tibias, indicating that inter-animal variation in response to PTH dosing—a finding consistent with our previous study[49]—and not radiation exposure is the root cause. The finding of proliferative endosteal bone is consistent with typical "early-stage" PTH-mediated bone modeling behavior, referred to as the "PTH anabolic window"[63] in which bone formation is most prominent,[64] followed by later stages of increased bone remodeling–induced bone resorption.[63]

The secondary objective of this study was to identify potential radiation dose impacts through the assessment of LER, cortical porosity parameters, cross-sectional cortical geometric

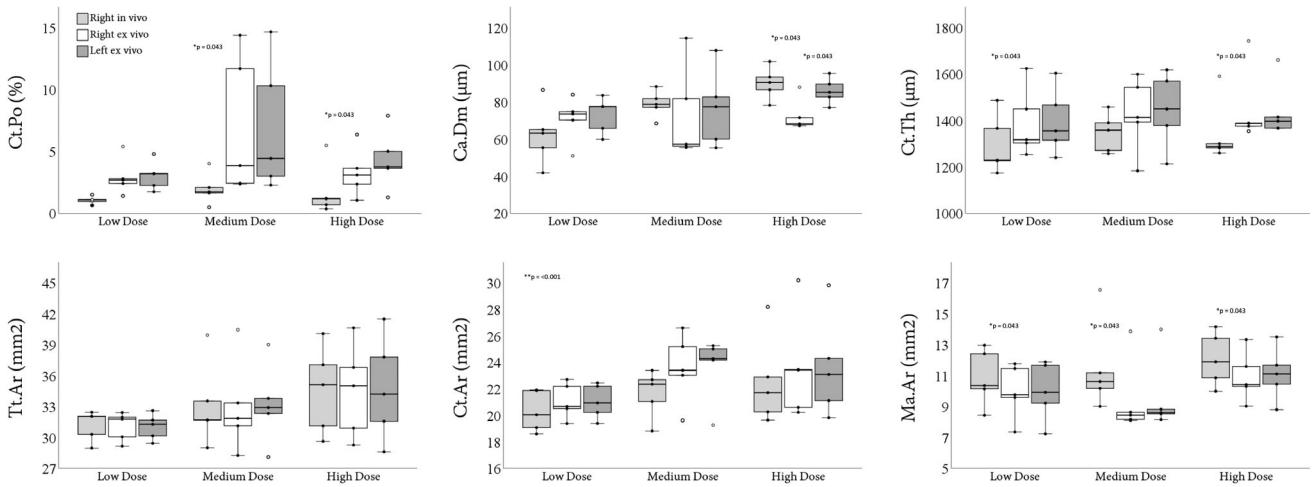

Fig. 6. Comparison of parameters among the in vivo (synchrotron radiation [SR] micro-CT—day 15) and ex vivo (micro-CT—day 29) scans of the right and contralateral left tibias for different radiation dose groups (low dose [1 Gy]; medium dose [2.5 Gy]; high dose [5 Gy]). Data are presented by box plots (right in vivo [light gray]; right ex vivo [white]; left ex vivo [dark gray]) with the mean (or median for nonparametric tests) for each individual rabbit plotted as solid circles and outliers plotted as open circles. $n = 5$. Repeated measures ANOVA (**$p < 0.05$) comparing tibia scans across the radiation dose groups was employed for normal data. Wilcoxon signed-rank test comparing tibia scans manually categorized by radiation dose group (*$p < 0.05$) was employed for non-normal data. Significance level was $\alpha = 0.05$. 3D measures (top row): Ct.Po = Cortical Porosity, Ca.Dm = Canal Diameter, and Ct.Th = Cortical Thickness. 2D measures (bottom row) Tt.ar = Total Area, Ct.Ar = Cortical Area, and Ma.Ar = Marrow Area.

parameters, and dynamic histomorphometric measures across the three radiation doses. Increased radiation dose equates to improved image quality (ie, better signal/contrast-to-noise ratio—see Supplemental Fig. S4; Fig. 4*A–C*), which we observed in our scans. Indeed, the noisy appearance of the low-dose group images carried through to the 3D segmentations, making them the most difficult to place cutting cone landmarks. Thus, while there was no difference in the precision of the registrations across the dose groups (Supplemental Table S1), for future applications of this approach, we plan to use the medium dose because it provided superior image quality relative to the low dose (Supplemental Fig. S4) and will be suitable for multiple adjacent in vivo scans with a slight region of overlap where the dose would be approximately 5 Gy. Ultimately, LER did not differ across radiation dose groups. Further, the lack of differences among the bone parameters between the in vivo imaged right and contralateral left tibias (other than Ca.Dm for the high-dose group; $p = 0.043$) is suggestive that, overall, the parameters of the imaging protocol employed for this study did not have an overt effect on the cortical bone in these rabbits within the timescale of the study—particularly for the low and medium doses. This conclusion is further supported by the fact that weight loss, consistent with this model system,[49] did not differ by dose group and other indications of distress such as changes to behavior, appetite, and water intake were not observed in any group. Some outcomes of the histomorphometric analysis superficially appear to suggest an impact of radiation dose between the limbs, with the in vivo imaged right tibia having lower remodeling rate (Ac.f, $p = 0.004$; a.Rm.Cr/Ct.Ar, $p = 0.006$), but this is the product of a difference in double-labeled osteons (dL.On/Ct.Ar, $p < 0.001$), which represent BMUs that were already active on day 15 and thus were already present within the bone at the time of in vivo imaging. This key point, combined with the fact that rate of closure of the BMU closing cones (On.MAR, $p = 0.727$) and the number of resorption cavities (Rs.N/Ct.Ar, $p = 0.171$; representing the initial phase of remodeling) did not differ between the limbs suggests radiation dose is not the cause of the differences between the sides. This finding is also consistent with a recent review[65] that reported radiation dose effects initially increase osteoclast activity and gradually decrease osteoblast activity in the weeks after exposure in animal models. Further research is needed to determine if rabbits consistently exhibit side differences in remodeling rate. Notably, the contralateral left limbs had remodeling rates very similar to those in our previous ex vivo study.[49]

Radiation effects in bone tissue have been reported as both a factor of dose and time, with previous studies reporting variable responses in rabbit bones exposed to a single dose (therapeutic X-ray) of 25, 50, and 100 Gy over a 4- 52-week observation period.[66] Exposure to a single dose of 35 Gy has been shown to increase porosity and decrease cortical area in the femora of rats at 14 and 18 weeks post-dosing.[67] Similarly, suppressed bone formation (4 weeks) and increased porosity (12 weeks) have also been reported in rabbits after a single exposure to 50 Gy.[68] Interestingly, timed analysis of rabbit tibias (7, 14, 21 days) post-exposure to a single dose of 30 Gy showed that the majority of impacted cortical parameters, including porosity, recovered to non-irradiated levels 14 and 21 days post-exposure, suggestive of a potential correlation between bone turnover recovery and time post-exposure.[69] Although the rabbits in our study had the added variable of PTH treatment, their cortices were subjected to non-therapeutic radiation doses and assessed after a shorter period (14 days) post in vivo imaging, which may explain why we found little evidence of significant radiation dose effects. Notably, in this study, we only reported the incident dose; however, since the synchrotron beam utilized here was monoenergetic, the absorbed dose in the bone tissue here is less than the case of polychromatic X-ray beam from X-ray tube

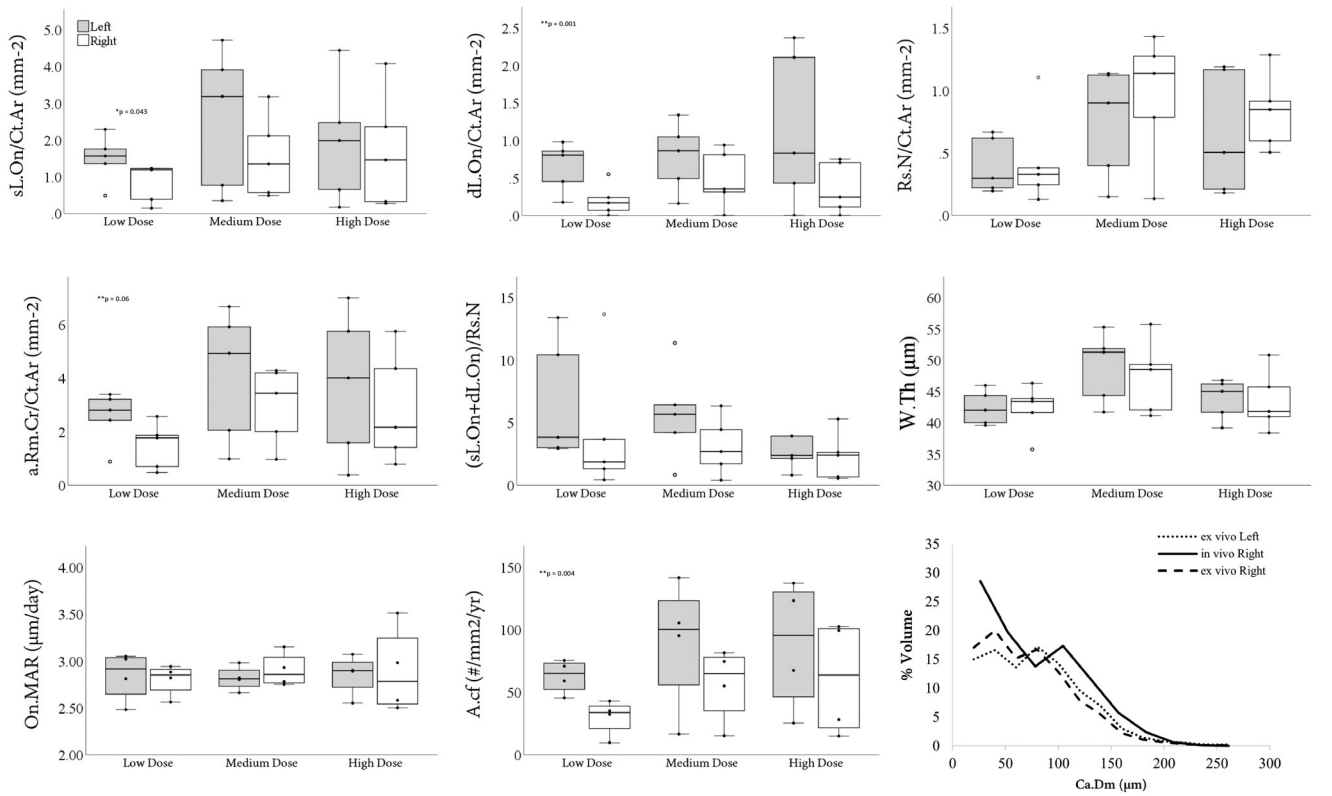

Fig. 7. Histomorphometric analyses of transverse cortical bone sections comparing the previously in vivo imaged right (white) and contralateral left (gray) tibias. Data are presented as box plots with the mean (or median for nonparametric tests) for each individual rabbit plotted as solid circles and outliers plotted as open circles. $n = 7$ except for On.MAR and Ac.f measures, where dL.On were not detectable in one rabbit from each radiation dose group (low dose, 1 Gy [$n = 4$]; medium dose, 2.5 Gy [$n = 4$]; high dose, 5 Gy [$n = 4$]). Repeated measures ANOVA (**$p < 0.05$) comparing left and right tibias across the radiation dose groups was employed for normal data. Wilcoxon signed-rank test comparing the right and left tibias manually categorized by radiation dose group (*$p < 0.05$) was employed for non-normal data. Significance level was $\alpha = 0.05$. For canal diameter (Ca.Dm), the plots reveal bimodal distributions of Ca.Dm sizes for all three groupings. The left peaks in the distributions reveal a large percentage of the porous canals at or near the resolution of the scans. The right peaks around 80 to 100 (ex vivo) and 120 (in vivo) µm represent the diameters of basic multicellular unit (BMU)-related remodeling spaces. sL.On = Single-Labeled Osteon; dL.On = Double-Labeled Osteon; Rs.N = Resorption Cavities; a.Rm.Cr = Active Remodeling Centers; Ct.Ar = Cortical Area; W.Th = Wall Thickness; On.MAR = Osteonal Mineral Apposition Rate; Ac.f = Activation Frequency.

sources. Future studies where bone tissues analyzed from rabbits euthanized several weeks to months post in vivo SR micro-CT scanning would provide further support for the findings of this study since radiation damage has been observed in the cortical bone of animals subjected to radiation several weeks to months post-exposure.[66,67]

A limitation of our experimental protocol is the lack of a non-PTH control group. In a previous study, we found that PTH increased remodeling rate (Ac.f) 14.2-fold versus SHAM rabbits[49]; therefore, with our 12.4 BMUs/rabbit, a matched control group ($n = 5$) may only have provided 0.9 BMUs/rabbit or 4 to 5 BMUs in total. A low, but highly variable, rate of baseline remodeling in normal rabbits was also confirmed in preliminary (unpublished) trials of our imaging protocol where one normal rabbit looked similar compared with our PTH-dosed animals and all others had little apparent remodeling. As our objective here was to introduce a novel approach for measuring LER, and not to test a biological hypothesis, we chose to not include a control group because of concerns focused on the ethical use of animals and cost. Also, while the intended use of PTH to increase the number of active BMUs for LER measures was achieved (eg, Ac.f for the sham OVH control group of our previous study was 4.04 BMUs/mm^2/yr[49] versus our values ranging from ~30 to 90 BMUs/mm^2/yr; see Table 5), the efficiency at which this was done resulted in: (i) co-registration issues, with one rabbit per group excluded for analysis and (ii) challenges locating classically shaped BMUs as PTH induced extensive and irregular remodeling (eg, Fig. 4*E*). Future application of the methodology could mitigate these limitations by potentially lowering the dose of PTH and/or increasing the size of FOV (eg, the adjacent scans discussed above) and thereby increasing the ability to locate suitable BMUs for analysis in PTH-dosed animals as well as other models (eg, OVH) and even control animals.[49]

A limitation of our protocol was the use of different imaging platforms (SR micro-CT versus micro-CT) for the two scans of each animal; however, doing so meant that we did not require additional (inherently limited) synchrotron beamtime for the second scan. Although it would increase the complexity of the experiment, including additional synchrotron beamtime, multiple in vivo assessments could certainly be entertained for future studies. Such an approach would be particularly powerful for looking at dynamic modulation of individual BMU activity over

Table 4. Right Versus Left Tibias: Ex Vivo Scans

				Right ex vivo versus left ex vivo									
				Low dose (1 Gy)			Medium dose (2.5 Gy)			High dose (5 Gy)			
				Mean ± SD (median)			Mean ± SD (median)			Mean ± SD (median)			
Parameter	ANOVA *p* side (right versus left)	ANOVA *p* interaction (side × dose)	Wilcoxon-signed rank *p*	R. ex vivo	L. ex vivo	Wilcoxon-signed rank *p*	R. ex vivo	L. ex vivo	Wilcoxon-signed rank *p*	R. ex vivo	L. ex vivo	Wilcoxon-signed rank *p*	R. ex vivo	L. ex vivo
Ct.Po (%)	0.212	—	—	2.93 ± 1.48	3.04 ± 1.16	—	6.94 ± 5.67	6.93 ± 5.35	—	3.29 ± 1.97	4.30 ± 2.41			
Ca.Dm (μm)	—	—	0.500	70.65 ± 12.15 (73.52)	72.77 ± 9.71 (77.41)	0.893	72.94 ± 25.62 (57.23)	76.57 ± 20.87 (77.34)	0.043*	72.49 ± 8.78 (68.21)	85.94 ± 7.04 (85.22)			
Ct.Th (μm)	—	—	0.686	1389.13 ± 149.67 (1316.81)	1395.87 ± 142.48 (1354.76)	0.345	1426.34 ± 161.32 (1412.85)	1445.71 ± 161.07 (1449.40)	0.893	1449.65 ± 164.37 (1387.88)	1440.93 ± 124.53 (1397.19)			
Tt.Ar (mm^2)	0.592	—	—	31.07 ± 1.40	31.03 ± 1.25	—	33.00 ± 4.57	33.22 ± 3.91	—	34.51 ± 4.57	34.73 ± 5.07			
Ct.Ar (mm^2)	—	—	0.893	21.09 ± 1.34 (20.66)	21.04 ± 1.29 (20.94)	0.893	23.56 ± 2.63 (23.40)	23.60 ± 2.47 (24.28)	0.686	23.58 ± 4.00 (23.42)	23.62 ± 3.87 (23.09)			
Ma.Ar (mm^2)	—	—	0.893	9.98 ± 1.76 (9.76)	9.98 ± 1.91 (9.92)	0.225	9.44 ± 2.48 (8.44)	9.62 ± 2.46 (8.61)	0.893	10.93 ± 1.62 (10.42)	11.10 ± 1.72 (11.11)			

Bone parameters compared between the ex vivo micro-CT (day 29) scan data for the previously in vivo imaged (right) and contralateral (left) control tibiae/dose group (n = 5). Values are reported as mean ± standard deviation. Median values are reported for those parameters where at least one dose group was not normally distributed. For normal data, repeated measures ANOVA was employed to compare the right ex vivo vs. left ex vivo tibiae results across the radiation dose groups. For non-normal data, Wilcoxon signed-rank tests were employed to compare the right ex vivo vs. left ex vivo tibiae results categorized by radiation dose group. Significance (*) level was $\alpha = 0.05$ for all tests. Ct.Po = Cortical Porosity, Ca.Dm = Canal Diameter, and Ct.Th = Cortical Thickness. 2D measures (bottom row) Tt.Ar = Total Area, Ct.Ar = Cortical Area, and Ma.Ar = Marrow Area

time. Synchrotron imaging can also be limiting regarding the amount/type of skeletal element that can be imaged—methodologically, it is more feasible to image distal limbs at an effective dose compared with the vertebrae, for example. This is not dissimilar to human in vivo imaging platforms such as high-resolution peripheral quantitative computed tomography (HR-pQCT), which is restricted to the metaphyseal regions of the radius and tibia.[70]

Finally, the rabbit model of cortical remodeling-related spatiotemporal behavior exhibited high levels of variation, particularly for Ct.Po and several of the histomorphometric measures. Such variation was manifested as outliers within the data; however, a comparison of the 3D parameters in which the outliers were removed did not alter the results and therefore all data were retained for analysis. Despite these limitations, when compared with small laboratory rodent models (eg, mice and rats), which do not naturally exhibit cortical bone remodeling,[51] the rabbit does display cortical remodeling similar to that observed in humans[52-54] and thus offers an excellent option for the study of cortical remodeling in vivo.

Data obtained from the direct, 4D measurement of LER could provide the ability to assess the morphology or shape of the BMU to investigate characteristics of the closing cone or the scale of the reversal-resorption zone,[7,11] which could have significant clinical relevance in humans. Osteoporosis treatments typically involve antiresorptive (inhibiting bone resorption activity, eg, bisphosphonates[71]) or anabolic (stimulating bone formation, eg, PTH[64]) therapies. That said, rare but substantial adverse side effects such as osteonecrosis of the jaw[72] or atypical femoral fracture[73] have been associated with antiresorptive therapies. In contrast, complicated drug delivery schedules associated with PTH (ie, intermittent versus continuous administration) can result in undesirable catabolic instead of expected anabolic effects. The methodology presented here provides a novel platform to better investigate BMU spatiotemporal modulation by OP drugs directly in a preclinical model for the first time. Thus, a unique opportunity exists to potentially reduce unwanted side effects via more gauged dosing regimens. If BMUs can be reduced in size, slowed in their progression, spatially constrained to avoid coalescence into larger pores, and closely coupled with balanced resorption and formation, bone strength can be more safely preserved or even increased—reducing the overall burden of OP. There is also potential application to investigate hypotheses regarding BMU spatiotemporal behavior in general. For example, BMUs are thought to actively target and steer remodeling toward areas of microdamage in the form of microcracks[1,74-76] and/or other mechanical stimuli such as strain,[77,78] strain-derived fluid flow,[79-81] and loading-induced hydrostatic pressure.[82] The approach demonstrated here thus holds great potential to also test these hypothesized relations for the first time empirically.

This study represents the first direct assessment of LER in 4D. We found LER values in rabbits to be lower than those previously reported (and often cited) for dogs but not inconsistent with limited inferred values for humans. Further, our results indicated that the imaging protocol employed did not have an overt impact on the cortical bone parameters of rabbits during the study time frame. The method developed within this study serves as a novel platform to further advance our fundamental understanding of BMU spatiotemporal regulation and its role in bone aging, adaptation, and disease.

Table 5. Cortical Bone Histomorphometric Parameters

				Right tibia versus left tibia								
				Low dose (1 Gy)			Medium dose (2.5 Gy)			High dose (5 Gy)		
				Mean ± SD (median)			Mean ± SD (median)			Mean ± SD (median)		
Parameter	ANOVA *p* side (right versus left)	ANOVA *p* interaction (side × dose)	Wilcoxon-signed rank *p*	R. tibia	L. tibia	Wilcoxon-signed rank *p*	R. tibia	L. tibia	Wilcoxon-signed rank *p*	R. tibia	L. tibia
sL.On/Ct.Ar (mm^{-2})	—	—	0.043*	0.83 ± 0.52 (1.18)	1.49 ± 0.66 (1.56)	0.080	1.54 ± 1.13 (1.35)	2.58 ± 1.93 (3.18)	0.686	1.70 ± 1.59 (1.45)	1.94 ± 1.68 (1.98)
dL.On/Ct.Ar (mm^{-2})	0.001*	—	—	0.20 ± 0.21	0.65 ± 0.33	—	0.48 ± 0.39	0.78 ± 0.46	—	0.36 ± 0.34	1.15 ± 1.04
Rs.N/Ct.Ar (mm^{-2})	0.171	—	—	0.44 ± 0.38	0.40 ± 0.23	—	0.95 ± 0.52	0.83 ± 0.31	—	0.83 ± 0.31	0.65 ± 0.50
a.Rm.Cr/Ct.Ar (mm^{-2})	0.006*	—	—	1.47 ± 0.87	2.54 ± 1.00	—	2.97 ± 1.44	4.10 ± 2.47	—	2.89 ± 2.09	3.74 ± 2.77
(sL.On + dL.On)/Rs.N	—	—	0.345	4.19 ± 5.43 (1.86)	6.42 ± 4.87 (3.82)	0.345	3.11 ± 2.33 (2.69)	5.70 ± 3.83 (5.67)	0.138	2.30 ± 1.92 (2.39)	9.41 ± 15.93 (2.37)
W.Th (μm)	0.617	—	—	42.17 ± 3.97	42.36 ± 2.76	—	47.33 ± 5.97	48.88 ± 5.65	—	43.52 ± 4.86	43.75 ± 3.24
On.MAR (μm/day)	0.727	—	—	2.80 ± 0.17	2.84 ± 0.26	—	2.90 ± 0.18	2.82 ± 0.13	—	2.89 ± 0.46	2.85 ± 0.22
Ac.f ($\#/mm^2$/year)	0.004*	—	—	29.97 ± 14.25	62.67 ± 13.41	—	56.53 ± 29.74	89.59 ± 52.53	—	61.18 ± 46.13	88.27 ± 51.67

Histomorphometric analyses of transverse cortical bone sections comparing the previously in vivo imaged right and contralateral left tibiae by radiation dose group (n = 5) except for On.MAR and Ac.f measures where double labelled osteons were not detectable in one rabbit from each radiation dose group (Low Dose; 1 Gy (n = 4) Medium Dose; 2.5 Gy; (n = 4); High Dose 5 Gy (n = 4) groups. Values are reported as mean ± standard deviation. Median values are reported for those parameters where at least one dose group was not normally distributed. For normal data, repeated measures ANOVA was employed to compare the right vs. left results across the radiation dose groups. For non-normal data, Wilcoxon signed-rank tests were employed to compare the right vs. left tibia results categorized by radiation dose group. Significance (*) level was $\alpha = 0.05$ for all tests. sL.On = Single Labelled Osteon; dL.On = Double Labelled Osteon; Rs.N = Resorption Cavities; a.Rm.Cr = Active Remodeling Centers; Ct.Ar = Cortical Area; W.Th = Wall Thickness; On.MAR = Osteonal Mineral Apposition Rate; Ac.f = Activation Frequency.

Disclosures

All authors state that they have no conflicts of interest.

Acknowledgments

Part or all of the research described in this article was performed at the Canadian Light Source, a national research facility of the University of Saskatchewan, which is supported by the Canada Foundation for Innovation (CFI), the Natural Sciences and Engineering Research Council (NSERC), the National Research Council (NRC), the Canadian Institutes of Health Research (CIHR), the Government of Saskatchewan, and the University of Saskatchewan. This specific research was primarily supported by a CIHR Catalyst Grant (FRN: 151724). We also acknowledge Dr. George Belev's significant contributions toward the implementation of the in vivo imaging portion of this research, as well as Gavin King for his assistance with production of images for the article. We also thank Dr. Ingrid Pickering and Dr. Olena Ponomarenko for their contributions of resources and time regarding the confocal histological analyses portion of this research. We also acknowledge Dr. Denver Marchiori for his assistance with the data processing for the revision of this article. Finally, the authors acknowledge the support of the University of Saskatchewan Laboratory Animals Service Unit (LASU), which was essential for the success of this research.

Authors' roles: KDH: conceptualization, data curation, formal analysis, investigation, methodology, project administration, visualization, writing–original draft, and writing–review & editing. ES: formal analysis, methodology, visualization, writing–original draft, and writing–review & editing. BDH: data curation, methodology, and writing–review & editing. AP: conceptualization, data curation, funding acquisition, investigation, methodology, visualization, writing–original draft, and writing–review & editing. NZ: data curation and writing–review & editing. TA: conceptualization, funding acquisition, methodology, and writing–review & editing. KJS: data curation, investigation, methodology, and writing–review & editing. PP: conceptualization, funding acquisition, methodology, writing–original draft, and writing–review & editing. DC: conceptualization, methodology, and writing–review & editing. DMLC: conceptualization, data curation, formal analysis, funding acquisition, investigation, methodology, project administration, supervision, validation, visualization, writing–original draft, and writing–review & editing.

Author Contributions

Kim Harrison: Conceptualization; data curation; formal analysis; investigation; methodology; project administration; visualization; writing – original draft; writing – review and editing. **Erika Sales:** Formal analysis; methodology; visualization; writing – original draft; writing – review and editing. **Beverly Hiebert:** Data curation; methodology; writing – review and editing. **Arash Panahifar:** Conceptualization; data curation; funding acquisition; investigation; methodology; visualization; writing – original draft; writing – review and editing. **Ning Zhu:** Data curation; writing – review and editing. **Terra Arnason:** Conceptualization; funding acquisition; methodology; writing – review and editing. **Kurtis J Swekla:** Data curation; investigation; methodology; writing – review and editing. **Peter Pivonka:** Conceptualization; funding acquisition; methodology; writing – original draft;

writing – review and editing. **Dean Chapman:** Conceptualization; methodology; writing – review and editing. **David Cooper:** Conceptualization; data curation; formal analysis; funding acquisition; investigation; methodology; project administration; supervision; validation; visualization; writing – original draft; writing – review and editing.

Data Availability Statement

The data supporting the findings of this study are available from the corresponding author upon reasonable request.

References

1. Burr DB. Targeted and nontargeted remodeling. Bone. 2002;30(1): 2-4.
2. Frost HM. Bone remodeling dynamics. By H. M. Frost, M.D. Springfield, Charles C Thomas Company, 1963. 175 pp., 184 references, 12 appendices, 40 figures. $8.50. Arthritis Rheumatism. 1964;7(5):545.
3. Frost H. The bone dynamics in osteoporosis and osteomalacia. 1966. Springfield, IL: Charles C Thomas.
4. Johnson L. Morphologic analysis of pathology. In Frost H, ed. Bone biodynamics. Boston: Little, Brown, and Company; 1964 pp 543-654.
5. Frost HM. Tetracycline-based histological analysis of bone remodeling. Calcif Tissue Res. 1969;3(3):211-237.
6. Parfitt AM. The physiologic and clinical significance of bone histomorphometric data. Bone Histomorphom Techn Interpret. 1983; 1983:143-223.
7. Delaisse JM, Andersen TL, Kristensen HB, Jensen PR, Andreasen CM, Søe K. Re-thinking the bone remodeling cycle mechanism and the origin of bone loss. Bone. 2020;141:115628.
8. Li L, Wang Z. Ovarian aging and osteoporosis. In Wang Z, ed. Aging and aging-related diseases: mechanisms and interventions. Singapore: Springer Singapore; 2018 pp 199-215.
9. Kenkre JS, Bassett J. The bone remodelling cycle. Ann Clin Biochem. 2018;55(3):308-327.
10. Andersen TL, Abdelgawad ME, Kristensen HB, et al. Understanding coupling between bone resorption and formation: are reversal cells the missing link? Am J Pathol. 2013;183(1):235-246.
11. Andreasen CM, Ding M, Overgaard S, Bollen P, Andersen TL. A reversal phase arrest uncoupling the bone formation and resorption contributes to the bone loss in glucocorticoid treated ovariectomised aged sheep. Bone. 2015;75:32-39.
12. Seeman E, Delmas PD. Bone quality—the material and structural basis of bone strength and fragility. N Engl J Med. 2006;354(21): 2250-2261.
13. Yousefzadeh N, Kashfi K, Jeddi S, Ghasemi A. Ovariectomized rat model of osteoporosis: a practical guide. EXCLI J. 2020;19:89-107.
14. Brommage R, Ohlsson C. Translational studies provide insights for the etiology and treatment of cortical bone osteoporosis. Best Pract Res Clin Endocrinol Metab. 2018;32(3):329-340.
15. Rochefort GY. The osteocyte as a therapeutic target in the treatment of osteoporosis. Therap Adv Musculoskel Dis. 2014;6(3):79-91.
16. Bjørnerem Å, Ghasem-Zadeh A, Bui M, et al. Remodeling markers are associated with larger intracortical surface area but smaller trabecular surface area: a twin study. Bone. 2011;49(6):1125-1130.
17. Rashki Kemmak A, Rezapour A. Economic burden of osteoporosis in the world: a systematic review. Med J Islam Repub Iran. 2020;34:154.
18. Bala Y, Zebaze R, Seeman E. Role of cortical bone in bone fragility. Curr Opin Rheumatol. 2015;27(4):406-413.
19. Cohen J, Harris WH. The three-dimensional anatomy of Haversian systems. J Bone Joint Surg. 1958;40(2):419-434.
20. Tappen NC. Three dimensional studies of resorption spaces and developing osteons. Am J Anat. 1977;149(3):301-317.
21. Robling AG, Stout SD. Morphology of the drifting osteon. Cells Tissues Organs. 1999;164(4):192-204.
22. Stout SD, Brunsden BS, Hildebolt CF, Commean PK, Smith KE, Tappen NC. Computer-assisted 3D reconstruction of serial sections of cortical bone to determine the 3D structure of osteons. Calcif Tissue Int. 1999;65(4):280-284.
23. Andersen TL, Sondergaard TE, Skorzynska KE, et al. A physical mechanism for coupling bone resorption and formation in adult human bone. Am J Pathol. 2009;174(1):239-247.
24. Andreasen CM, Delaisse J-M, van der Eerden BCJ, van Leeuwen JPTM, Ding M, Andersen TL. Understanding age-induced cortical porosity in women: is a negative BMU balance in quiescent osteons a major contributor? Bone. 2018;117:70-82.
25. Lassen NE, Andersen TL, Pløen GG, et al. Coupling of bone resorption and formation in real time: new knowledge gained from human Haversian BMUs. J Bone Miner Res. 2017;32(7):1395-1405.
26. Turner C, Burr D, Jee WS, et al. Tribute to Harold M. Frost M.D. J Musculoskelet Neuronal Interact. 2004;4(4):347-356.
27. Mohsin S, Taylor D, Lee T. Three-dimensional reconstruction of Haversian systems in ovine compact bone. Eur J Morphol. 2002; 40(5):309-315.
28. Jaworski ZF, Lok E. The rate of osteoclastic bone erosion in Haversian remodeling sites of adult dog's rib. Calc Tissue Re J Art. 1972;10(1): 103-112.
29. Jaworski ZF, Lok E, Wellington JL. Impaired osteoclastic function and linear bone erosion rate in secondary hyperparathyroidism associated with chronic renal failure. Clin Orthop Relat Res. 1975;107: 298-310.
30. Takahashi H, Norimatsu H. The longitudinal and transverse rate of resorption of the Haversian system in canine bone. In Jaworski JF, ed. Bone morphometry. Ottawa: University of Ottawa Press; 1976 p 143.
31. Buenzli PR, Pivonka P, Smith DW. Spatio-temporal structure of cell distribution in cortical bone multicellular units: a mathematical model. Bone. 2011;48(4):918-926.
32. Buenzli PR, Jeon J, Pivonka P, Smith DW, Cummings PT. Investigation of bone resorption within a cortical basic multicellular unit using a lattice-based computational model. Bone. 2012;50(1):378-389.
33. Ryser MD, Komarova SV, Nigam N. The cellular dynamics of bone remodeling: a mathematical model. SIAM J Appl Math. 2010;70(6): 1899-1921.
34. David V, Laroche N, Boudignon B, et al. Noninvasive in vivo monitoring of bone architecture alterations in Hindlimb-unloaded female rats using novel three-dimensional microcomputed tomography. J Bone Miner Res. 2003;18(9):1622-1631.
35. Waarsing J, Day J, Van Der Linden J, et al. Detecting and tracking local changes in the tibiae of individual rats: a novel method to analyse longitudinal in vivo micro-CT data. Bone. 2004;34(1):163-169.
36. Cooper DM, Turinsky AL, Sensen CW, Hallgrimsson B. Quantitative 3D analysis of the canal network in cortical bone by micro-computed tomography. Anat Rec B New Anat. 2003;274(1):169-179.
37. Altman AR, Tseng W-J, de Bakker CMJ, et al. Quantification of skeletal growth, modeling, and remodeling by in vivo micro computed tomography. Bone. 2015;81:370-379.
38. Li Z, Kuhn G, von Salis-Soglio M, et al. In vivo monitoring of bone architecture and remodeling after implant insertion: the different responses of cortical and trabecular bone. Bone. 2015;81:468-477.
39. Bott KN, Yumol JL, Peters SJ, Ward WE. Sex-specific responses in trabecular and cortical microstructure of tibia due to repeated irradiation from micro-computed tomography in adult CD-1 mice. Bone Rep. 2020;12:100232.
40. Longo AB, Salmon PL, Ward WE. Comparison of ex vivo and in vivo micro-computed tomography of rat tibia at different scanning settings. J Orthop Res. 2017;35(8):1690-1698.
41. Willie BM, Birkhold AI, Razi H, et al. Diminished response to in vivo mechanical loading in trabecular and not cortical bone in adulthood of female C57Bl/6 mice coincides with a reduction in deformation to load. Bone. 2013;55(2):335-346.
42. Klinck RJ, Campbell GM, Boyd SK. Radiation effects on bone architecture in mice and rats resulting from in vivo micro-computed tomography scanning. Med Eng Phys. 2008;30(7):888-895.

43. Laperre K, Depypere M, van Gastel N, et al. Development of micro-CT protocols for in vivo follow-up of mouse bone architecture without major radiation side effects. Bone. 2011;49(4):613-622.
44. Matsumoto T, Nishikawa K, Tanaka M, Uesugi K. In vivo CT quantification of trabecular bone dynamics in mice after sciatic neurectomy using monochromatic synchrotron radiation. Calcif Tissue Int. 2011; 88(5):432-441.
45. Ford NL, Thornton MM, Holdsworth DW. Fundamental image quality limits for microcomputed tomography in small animals. Med Phys. 2003;30(11):2869-2877.
46. Oliviero S, Giorgi M, Laud PJ, Dall'Ara E. Effect of repeated in vivo microCT imaging on the properties of the mouse tibia. PLoS One. 2019;14(11):e0225127.
47. Zhou S-A, Brahme A. Development of phase-contrast X-ray imaging techniques and potential medical applications. Phys Med. 2008; 24(3):129-148.
48. Pratt IV, Belev G, Zhu N, Chapman LD, Cooper DML. In vivo imaging of rat cortical bone porosity by synchrotron phase contrast micro computed tomography. Phys Med Biol. 2015;60(1):211.
49. Harrison KD, Hiebert BD, Panahifar A, et al. Cortical bone porosity in rabbit models of osteoporosis. J Bone Miner Res. 2020;35(11):2211-2228.
50. Turner RT, Maran A, Lotinun S, et al. Animal models for osteoporosis. Rev Endocr Metab Disord. 2001;2(1):117-127.
51. Lelovas PP, Xanthos TT, Thoma SE, Lyritis GP, Dontas IA. The laboratory rat as an animal model for osteoporosis research. Comp Med. 2008;58(5):424-430.
52. Pazzaglia UE, Bonaspetti G, Rodella LF, Ranchetti F, Azzola F. Design, morphometry and development of the secondary osteonal system in the femoral shaft of the rabbit. J Anat. 2007;211(3):303-312.
53. Pazzaglia UE, Congiu T, Raspanti M, Ranchetti F, Quacci D. Anatomy of the intracortical canal system: scanning electron microscopy study in rabbit femur. Clin Orthop Relat Res. 2009;467(9):2446-2456.
54. Pazzaglia UE, Zarattini G, Giacomini D, Rodella L, Menti AM, Feltrin G. Morphometric analysis of the canal system of cortical bone: an experimental study in the rabbit femur carried out with standard histology and micro-CT. Anat Histol Embryol. 2010;39(1):17-26.
55. Yamane H, Takakura A, Shimadzu Y, et al. Acute development of cortical porosity and endosteal naive bone formation from the daily but not weekly short-term administration of PTH in rabbit. PLoS One. 2017;12(4):e0175329.
56. Hirano T, Burr DB, Cain RL, Hock JM. Changes in geometry and cortical porosity in adult, ovary-intact rabbits after 5 months treatment with LY333334 (hPTH 1-34). Calcif Tissue Int. 2000;66(6):456-460.
57. Hirano T, Burr DB, Turner CH, Sato M, Cain RL, Hock JM. Anabolic effects of human biosynthetic parathyroid hormone fragment (1-34), LY333334, on remodeling and mechanical properties of cortical bone in rabbits. J Bone Miner Res. 1999;14(4):536-545.
58. Zebaze R, Takao-Kawabata R, Peng Y, et al. Increased cortical porosity is associated with daily, not weekly, administration of equivalent doses of teriparatide. Bone. 2017;99:80-84.
59. Santangelo B, Micieli F, Marino F, et al. Plasma concentrations and sedative effects of a dexmedetomidine, midazolam, and butorphanol combination after transnasal administration in healthy rabbits. J Vet Pharmacol Ther. 2016;39(4):408-411.
60. Voor MJ, Yang S, Burden RL, Waddell SW. In vivo micro-CT scanning of a rabbit distal femur: repeatability and reproducibility. J Biomech. 2008;41(1):186-193.
61. Glüer CC, Blake G, Lu Y, Blunt BA, Jergas M, Genant HK. Accurate assessment of precision errors: how to measure the reproducibility of bone densitometry techniques. Osteoporos Int. 1995;5(4):262-270.
62. Mashiba T, Burr DB, Turner CH, Sato M, Cain RL, Hock JM. Effects of human parathyroid hormone (1-34), LY333334, on bone mass, remodeling, and mechanical properties of cortical bone during the first remodeling cycle in rabbits. Bone. 2001;28(5):538-547.
63. Silva BC, Bilezikian JP. Parathyroid hormone: anabolic and catabolic actions on the skeleton. Curr Opin Pharmacol. 2015;22:41-50.
64. Ng PY, Ong AJ, Gale LS, Dass CR. Treatment of bone disorders with parathyroid hormone: success and pitfalls. Pharmazie. 2016;71(8): 427-433.
65. Costa S, Reagan MR. Therapeutic irradiation: consequences for bone and bone marrow adipose tissue. Front Endocrinol Mini Rev. 2019; 10:587.
66. Takahashi S, Sugimoto M, Kotoura Y, Sasai K, Oka M, Yamamuro T. Long-term changes in the Haversian systems following high-dose irradiation. An ultrastructural and quantitative histomorphological study. J Bone Joint Surg Am. 1994;76(5):722-738.
67. Maeda M, Bryant MH, Yamagata M, Li G, Earle JD, Chao EY. Effects of irradiation on cortical bone and their time-related changes. A biomechanical and histomorphological study. J Bone Joint Surg Am. 1988; 70(3):392-399.
68. Sugimoto M, Takahashi S, Toguchida J, Kotoura Y, Shibamoto Y, Yamamuro T. Changes in bone after high-dose irradiation. Biomechanics and histomorphology. J Bone Joint Surg Br. 1991;73(3): 492-497.
69. Borges JS, Rabelo GD. Cortical bone modifications after radiotherapy: cortex porosity and osteonal changes evaluated over time. Braz Dent J. 2021;32(1):9-15.
70. Mikolajewicz N, Bishop N, Burghardt AJ, et al. HR-pQCT measures of bone microarchitecture predict fracture: systematic review and meta-analysis. J Bone Miner Res. 2020;35(3):446-459.
71. Russell RG, Watts NB, Ebetino FH, Rogers MJ. Mechanisms of action of bisphosphonates: similarities and differences and their potential influence on clinical efficacy. Osteoporos Int. 2008;19(6):733-759.
72. Migliorati CA, Siegel MA, Elting LS. Bisphosphonate-associated osteonecrosis: a long-term complication of bisphosphonate treatment. Lancet Oncol. 2006;7(6):508-514.
73. Gedmintas L, Solomon DH, Kim SC. Bisphosphonates and risk of subtrochanteric, femoral shaft, and atypical femur fracture: a systematic review and meta-analysis. J Bone Miner Res. 2013;28(8):1729-1737.
74. Martin RB. Is all cortical bone remodeling initiated by microdamage? Bone. 2002;30(1):8-13.
75. Martin RB. Targeted bone remodeling involves BMU steering as well as activation. Bone. 2007;40(6):1574-1580.
76. Parfitt AM. Targeted and nontargeted bone remodeling: relationship to basic multicellular unit origination and progression. Bone. 2002; 30(1):5-7.
77. Smit TH, Burger EH. Is BMU-coupling a strain-regulated phenomenon? A finite element analysis. J Bone Miner Res. 2000;15(2):301-307.
78. van Oers RFM, Ruimerman R, van Rietbergen B, Hilbers PAJ, Huiskes R. Relating osteon diameter to strain. Bone. 2008;43(3): 476-482.
79. Smit TH, Burger EH, Huyghe JM. A case for strain-induced fluid flow as a regulator of BMU-coupling and osteonal alignment. J Bone Miner Res. 2002;17(11):2021-2029.
80. Burger EH, Klein-Nulend J, Smit TH. Strain-derived canalicular fluid flow regulates osteoclast activity in a remodelling osteon—a proposal. J Biomech. 2003;36(10):1453-1459.
81. Estermann S-J, Scheiner S. Multiscale modeling provides differentiated insights to fluid flow-driven stimulation of bone cellular activities. Front Phys. 2018;6:76.
82. Scheiner S, Pivonka P, Hellmich C. Poromicromechanics reveals that physiological bone strains induce osteocyte-stimulating lacunar pressure. Biomech Model Mechanobiol. 2016;15(1):9-28.
83. Harrison K, Sales E, Hiebert B, et al. Direct four-dimensional assessment of cortical bone basic multicellular unit longitudinal erosion rate in PTH-dosed rabbits: a novel synchrotron X-ray imaging approach. Am Soc Bone Miner Res Ann Meet. 2020; 35:275.
84. Harrison K. A novel in vivo synchrotron radiation micro-CT imaging platform for the direct tracking of remodeling events in cortical bone. Thesis, 2021:199.